**To cite this version :**

# Study on the effect of cuprite content on the electrical and CO$_2$ sensing properties of cuprite-copper ferrite nanopowder composites

T.P. Sumangala [a, b], Yohann Thimont [a], Valérie Baco-Carles [a], Lionel Presmanes [a], Corine Bonningue [a], Isabelle Pasquet [a], Philippe Tailhades [a], Antoine Barnabé [a, *]

[a] CIRIMAT, Université de Toulouse, CNRS, INPT, UPS, Université Toulouse 3 Paul Sabatier, 118 route de Narbonne, 31062 Toulouse Cedex 9, France
[b] Metallurgical Engineering and Materials Science Department, Indian Institute of Technology Bombay, IIT Powai, Mumbai 400076, India

## ABSTRACT

The paper reports the synthesis and characterization of cuprite/copper ferrite nanopowder composites. The composites were synthesized using co-precipitation with oxalates precursor route. The phase and microstructure of the powder samples were characterized using X-ray diffraction, BET surface area analyzer and scanning electron microscopy. The powders were fabricated to device using a simple and efficient shaping technique. These devices were used further to carry out electrical property measurements in various atmospheres. The type of charge carriers were found by noting the sense of change in resistance when the air atmosphere on the sample was replaced with argon. CO$_2$ responses were reported for the whole series of composites. The effect of cuprite concentration on the CO$_2$ sensing performance was found to be independent of cuprite concentration up to certain limits (70%$^{at}$).

## 1. Introduction

Oxide-based nanostructured composites have demonstrated superior performance in a wide variety of applications ranging, for instance, from transparent electronics [1] to gas sensors [2]. Among them, cuprite (copper (II) oxide CuO) is a very interesting metal oxide as it is useful for various applications including lithium-ion batteries, supercapacitors, gas and electrochemical sensors, solar cells, catalysis, photo detectors, super hydrophobic surfaces and field emission display [3]. Spinel ferrites (MFe$_2$O$_4$) are metal oxides which have been studied for several decades due to their magnetic and microwave properties. After the advent of nanotechnology, spinel ferrites have resumed their attention and have potential applications in biomedical industry, catalysis and sensors [4,5]. They have potential bio medical applications ranging from magnetic targeted drug delivery for cancer treatments to treatments like hyperthermia [6]. Ferrites have been widely investigated as gas sensors. Almost all ferrites, MFe$_2$O$_4$ (with M = Cd, Co, Cu, Mg, Ni and Zn) has been observed to have interesting gas sensing properties [7–12]. Among the various ferrites, copper ferrite has been studies for its response towards hydrogen, ethanol and Liquefied Petroleum Gas (LPG) [7,13]. Spinel ferrites have also been used in combination with graphene oxide for sensing acetone [14].

Carbon dioxide, one of the constituents in air has many adverse effects on human health and atmosphere (due to its greenhouse gas behavior). Carbon dioxide, on the other hand, is useful to trace fire accidents and/or human presence and activities. Thus the detection of CO$_2$ is interesting in health, environmental and technological sectors. However, despite of its huge interests, CO$_2$ detection by Metal Oxide Semiconductor (MOS) sensors technology is challenging because of the low reactivity of CO$_2$. The surface interaction affecting the band structure and charge carrier concentration of the material appears to be insufficient to invoke significant sensing response. The lack of suitable active materials for CO$_2$ detection is the biggest challenge that current MOS sensors are facing. Various materials (monoxides, mixed oxides, halogenides, …) with different fabrication methods have been investigated to produce semiconductor CO$_2$ gas sensors, but generally with poor performance due to low response and/or high cross-sensitivity [15–17]. The use of perovskite/copper monoxide composites for sensing carbon monoxide have been already reported [18] with more promising results and was further studied by various research

* Corresponding author.
  E-mail address: barnabe@chimie.ups-tlse.fr (A. Barnabé).

groups [19–21] for such application. The sensing of $CO_2$ using alternative thin film composite made of spinel copper ferrite/copper monoxide was also proposed by our group [22]. It was observed that the composites can lead to particles with different type of charge carriers (p and n) in close proximity and hence could be interesting for sensing [23]. For the $BaTiO_3$-based composites, Ishihara et al. [18] have already demonstrated that the $CO_2$ sensing characteristics strongly depend on the kind of oxides mixed with $BaTiO_3$, but the effect of the concentration of metal oxide in the spinel ferrite/metal oxide composites on the gas sensing properties has not been studied yet. It would then be interesting to perform a systematic study on the effect of copper oxide content in the $CO_2$ sensing performance of copper ferrite/copper oxide composite.

Ferrites nanoparticles have been used in pellet, rod, thin and thick film forms for their sensor application [8,24,25]. Thin film processing is difficult to carry out for testing various compositions. Despite of its shaping process simplicity, compaction of nanopowders in pellet form has the disadvantage of the reduction in available active surface in the characterization of sensing properties.

In this paper, we report a novel method for elaborating and using directly nanopowders in the form of a device. We report here a study on the influence of cuprite content on the structural, microstructural, electrical and $CO_2$ sensing properties of the entire series of composite $CuO/CuFe_2O_4$ prepared by co-precipitation method.

## 2. Experimental details

### 2.1. Synthesis of the $CuO/CuFe_2O_4$ composite materials

Stoichiometric amounts of metal chlorides (copper chloride and ferrous chloride) in the $0.33 \leq Cu/(Cu + Fe) \leq 1$ ratio were dissolved in a mixture of water ($60\%^{vol}$) and ethylene glycol ($40\%^{vol}$) to form a 2 M solution, using a magnetic stirrer at 20 °C. About 1% of hydrochloric acid (HCl) was added to the metallic salts to prevent oxidation of ferrous ion (Sol1). Simultaneously, oxalic acid with a 7 wt% excess with respect to the metal ions was dissolved in ethanol (0.5 M) using mechanical stirrer at a speed of 300 rpm (Sol2). Sol1 was quickly added (rate of 60 ml/min) to Sol2 using a peristaltic pump and was stirred mechanically for 1 h. The resulting suspension was centrifuged with a speed of 3500 rpm for 10 min. This was followed by three consecutive washing with de-ionized water under mechanical stirring for 30 min and centrifugation with 3500 rpm for 10 min. This was continued until the chlorides have been removed. A final washing was performed following the same protocol with ethanol. Then the precursor was dried in oven at 80 °C for 8 h. The nature of the oxalate precursor (mixed oxalate or mixture of oxalates) was determined by powder X-Ray Diffraction (XRD) analysis using a D4-Endeavor Bruker diffractometer equipped with a copper anode and a LynxEye 2D detector. Temperature X-ray diffraction measurements were carried out in an Antonn Paar HTK1200 N oven chamber with a D8-Advanced Bruker diffractometer equipped with identical anode and detector.

The oxalate was then decomposed in air by heating to 250 °C with a heating rate of 50 °C/hour for Cu/Fe oxalates and with a heating rate of 10 °C/hour for copper oxalate. These heating rates were required to prevent the formation of $\alpha$-$Fe_2O_3$ for Cu/Fe oxalates, and to prevent the formation of $Cu_2O$ along with CuO for pure copper oxalate. To finish the reaction, the decomposed products were calcined at 760 °C for 4 h except for pure copper ferrite which was calcined at 780 °C for 4 h. The nature of the phase of the powder was checked using XRD. The Cu/Fe ratio of the samples were found using Bruker S2-Ranger X-Ray Fluorescence (XRF) spectrometer equipped with helium atmosphere sample chamber.

The cationic ratio was further confirmed using a JEOL JSM-6400 Scanning Electron Microscope (SEM), associated with an Oxford Instruments X-Max Si-Li detector for qualitative (Cu and Fe elements) and semi-quantitative (Cu/Fe ratio) Energy Dispersive Spectroscopy (EDS) analysis. The quantification of crystalline phases was performed by Rietveld refinement implemented in the Fullprof program. The microstructure analysis was performed using a BET single point Micromeritics Automate 23 surface area analyzer and a JEOL JSM-6400 SEM.

### 2.2. Device fabrication for gas sensing measurements

The device for gas sensing was fabricated on alumina substrate of 15 mm × 15 mm dimension. The electrode for the device was porous silver coated on the substrate. This was done by coating silver oxalate mixed in ethylene glycol on the substrate and decomposing the oxalate to metallic silver according to the procedure used for soldering with oxalate-based materials [26]. After coating, the substrate was then kept in vacuum for 24 h and was subsequently heated to 800 °C to obtain silver without crack. A heating rate of 50 °C/hour was used up to 150 °C and then the heating rate was increased to 150 °C/hour. Once 800 °C was reached the sample was allowed to cool normally in the furnace.

The sensing material (the metal oxide) was grind using a mortar and pestle and mixed in ethylene glycol. This paste was then coated on the substrate with electrode. This was again kept in vacuum for 24 h and was then heated to 780 °C for 1 h with a heating rate of 150 °C/hour and was allowed to cool normally in the furnace. The temperature of 780 °C was chosen so that the second thermal treatment on the powder does not have any impact on its microstructure. Fig. 1 gives the schematic and the SEM micrograph of the device.

The electrical properties of the sample were studied on this device by varying the temperature using a two probes method and
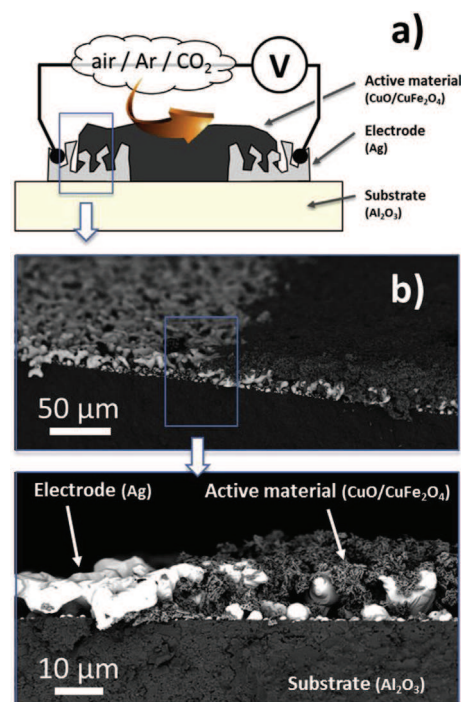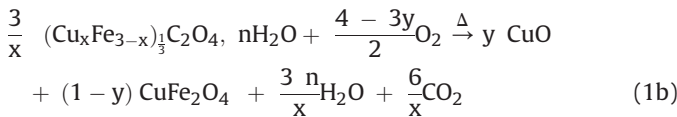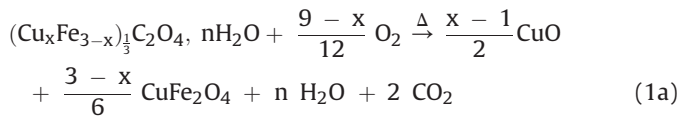


**Fig. 1.** a) Schematic representation of the device fabricated from various nanopowder composites for performing electrical measurement in controlled atmosphere and b) corresponding SEM micrographs.

a Keithley 2000 multimeter. The response of the samples to the change in the gaseous environment (air, argon and carbon dioxide) was recorded using a specialized cell from Linkam Scientific instruments (UK). Dry air (0% humidity), Ar and $CO_2$ (5000 ppm, balance dry air) were the gases used. Dry air and $Ar/CO_2$ was alternately passed into the cell with a flow rate of 100 sccm. The in-situ variation in resistance with the change in gaseous environment was measured using a Keithley 2400 source meter and was recorded in PC using data acquisition with National Instrument interface (USA) and Labview software. The response of the devices to $CO_2$ was calculated as $S (\%) = \frac{\Delta R}{R_{air}}$, where $R_{air}$ is the resistance in air and $\Delta R = R_{gas} - R_{air}$ is the change in resistance in the presence of test gas at a given temperature. The accuracy of the measurement was estimated by taking the standard deviation over multiple cycles on few representative samples.

# 3. Results and discussions

## 3.1. Structural characterization

XRD was performed on all the synthesized oxalates. From the XRD patterns, it was seen that the oxalate formed were mixed oxalates $(Cu_xFe_{3-x})_{1/3}C_2O_4$, $nH_2O$ with $1 \leq x \leq 1.35$ and $n = 0.5$ when the relative copper atomic content $\frac{Cu}{Cu+Fe} = \frac{x}{3} \leq 0.45$. When $\frac{Cu}{Cu+Fe} = \frac{x}{3} \geq 0.45$, the precipitation resulted in the formation of a mixture of two mixed copper-iron oxalates. After thermal decomposition it resulted in the formation of pure $CuFe_2O_4$ when $x = 1$ and a mixture of $CuFe_2O_4$ and $CuO$ when $x > 1$(Equation (1a)). Based on the refined lattice parameters, the copper ferrite spinel phase is assumed to be stoichiometric with a cationic ratio; Cu/Fe = 0.5. The amount of cuprite (y) is then expressed as $y = \frac{(x-1)/2}{x/3}$ which corresponds to the molar percentage of copper ions in cuprite compared to the total Cu ion content in the oxalate (Equation (1b)).

$$(Cu_xFe_{3-x})_{\frac{1}{3}}C_2O_4, nH_2O + \frac{9-x}{12}O_2 \xrightarrow{\Delta} \frac{x-1}{2}CuO$$
$$+ \frac{3-x}{6}CuFe_2O_4 + n\ H_2O + 2\ CO_2 \tag{1a}$$

$$\frac{3}{x}\ (Cu_xFe_{3-x})_{\frac{1}{3}}C_2O_4, nH_2O + \frac{4-3y}{2}O_2 \xrightarrow{\Delta} y\ CuO$$
$$+ (1-y)CuFe_2O_4 + \frac{3}{x}nH_2O + \frac{6}{x}CO_2 \tag{1b}$$

The content of copper oxide phase in each sample (y) was estimated using Rietveld refinement performed on all the samples. This value was further confirmed using EDS and XRF wherein the relative copper atomic percent (x/3) was measured and converted to y value as expressed earlier. Table 1 gives the y values obtained using these three techniques. The average of these values was taken as the CuO content in these samples. All the samples were named

based on the copper oxide content. Thus pure copper ferrite was termed as y000, pure copper oxide as y100, sample with 39% copper oxide was termed as y039 and so on.

Fig. 2 shows the XRD patterns of all the samples measured at room temperature. From Fig. 2 and Rietveld refinement, it could be seen that the sample y000 corresponds to tetragonal copper ferrite (space group I $4_1$/a m d with a = 5.8068(3)Å and c = 8.7128(5)Å, i.e. with a tetragonal distortion $c/_{a\sqrt{2}} \approx 1.06$) and sample y100 corresponds to cuprite (space group C 2/c with a = 4.6828(4)Å, b = 3.4224(4)Å, c = 5.1277(4)Å and β = 99.46(3)°). As we move from y000 to y100, the characteristic peaks of CuO start appearing as for instance near 39° and 49° corresponding to (200) & (111) and (−202) planes respectively. At the same time, the characteristic Bragg's peaks of the tetragonal copper ferrite tends to decrease and completely vanishes for y100. The scale factors of both phases could be determined by Rietveld refinement and this allows us to determine the exact proportion of cuprite in the whole sample in the entire series from y000 to y100 [27]. These values are reported in Table 1, as the percentage of CuO phase (y). The structural refinement also confirms that the increase in copper content affects only the proportion of the CuO phases and does not change the stoichiometry of the spinel phase because the lattice parameters of both phases remain unchanged in the whole series.

## 3.2. Microstructural characterization

The specific surface area of the samples measured using single point BET surface area method is also shown in Table 1. From Table 1, it could be seen that the specific surface area of all the samples is in the same range and shows almost a continuous decrease when increasing CuO content. The average particle size d assuming a spherical shape (form factor = 6) and calculated from the specific surface following Equation (2) is also given in Table 1.

$$d = \frac{6}{S_w \times \rho} \tag{2}$$

In this equation, $S_w$ represents the BET surface area in $m^2\ g^{-1}$ and ρ the volumic mass in $g.cm^{-3}$. The average particle size d shows almost a continuous increase from around 0.4 μm for pure $CuFe_2O_4$ to around 1.4 μm for CuO particles.

Fig. 3 gives the SEM micrographs of copper ferrite, copper oxide and two intermediate samples. From Fig. 3a, it could be seen that for copper ferrite (y000), the individual crystallites of around 0.2–0.5 μm in diameter are combined to form elongated particles and exhibit a spongy nature on pristine material. The micrograph of y000 powder on device proves that the microstructure of the sample remains the same. From the micrograph of composites, y052 (Fig. 3b) and y082 (Fig. 3c), we could see that there exist particles with two different geometry. There are elongated particles as seen in case of y000 (copper ferrite) and there are bigger spherical particles of around 1–2 μm in diameter. From these

**Table 1**
Quantification of CuO phase in all samples.

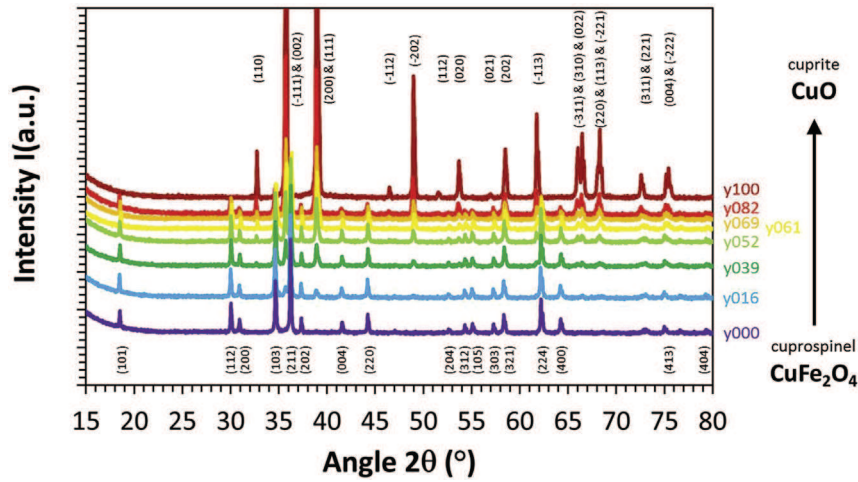| Sample name | %$^{at}$ of CuO in sample (y) | | | Specific surface area Sw ($m^2$/g) | Average particle size calculated from Sw (μm) |
|---|---|---|---|---|---|
| | Cu/Fe by XRF | Cu/Fe by EDS | y CuO by XRD | | |
| y000 | | | 0,00 | 2.6 | 0.43 |
| y016 | 0,13 | 0,18 | 0,17 | 2.4 | 0.45 |
| y039 | 0,39 | 0,39 | 0,40 | 2.6 | 0.40 |
| y052 | 0,52 | 0,52 | 0,52 | 1.9 | 0.54 |
| y061 | 0,60 | 0,63 | 0,61 | 1.7 | 0.59 |
| y069 | 0,66 | 0,71 | 0,70 | 1.6 | 0.62 |
| y082 | 0,81 | 0,85 | 0,82 | 1.5 | 0.65 |
| y100 | | | 1,00 | 0.7 | 1.36 |

**Fig. 2.** XRD patterns of the whole series of composite CuO/CuFe$_2$O$_4$.
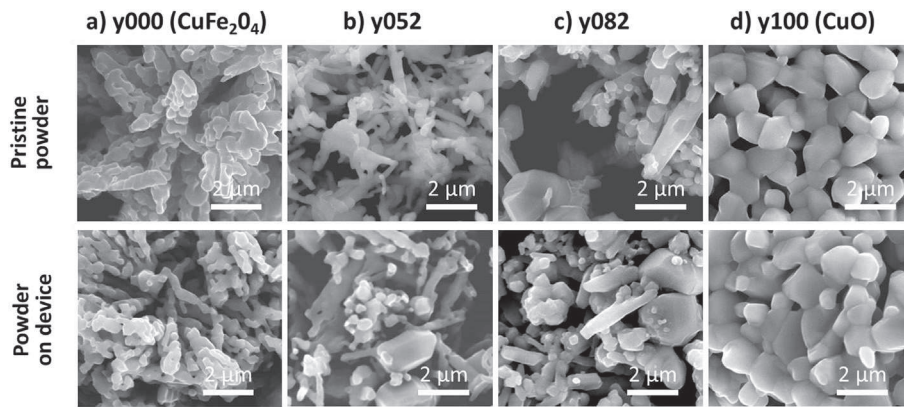


**Fig. 3.** Pristine powder and powder on device SEM micrographs of a) copper ferrite (y000), b) and c) copper ferrite/copper oxide composites (y052 and y082) and d) copper oxide (y100).

figures, it could be seen that the size of the spherical particles are higher than that of elongated particles. From the SEM image of y100 (CuO) shown in Fig. 3d, we see that there exist only one type of particle which are spherical in structure. This shows that the spherical particles seen in the composites are copper oxide particles. This was further confirmed by doing EDS analysis on the two different types of particles that existed in the composite samples. EDS results showed that the circular particles belong to copper oxide and the elongated to that of copper ferrite. Thus in composites, there exists particles with two distinct geometry and chemical composition corresponding to the two phases present in good accordance with XRD results. The overall increase in the particle size as it has been highlighted by the BET measurements (Table 1) could be attributed to the increase in the proportion of cuprite, which has bigger particles in comparison with copper ferrite. It could also be seen that the device formation does not change significantly the morphology or porosity inherent in the powder samples.

### 3.3. Electrical characterization

Fig. 4a shows the Arrhenius plot obtained for all the samples in the temperature range 150–450 °C, the heating and cooling cycle of samples with pure phases y000 and y100 is given in Fig. 4b along with the change in lattice parameter of y000 with temperature.

From Fig. 4a, it could be seen that for all samples, resistance decreases continuously with the increase in temperature. This confirms the semiconducting nature of all the samples. It could also be seen that the resistance of the samples y000 - y082 are in the same range. However, the resistance of y100 is much lower ($\approx 100$ times) than all other samples. All samples exhibit a linear behavior in the temperature range 150 to $\approx 370$ °C. In case of pure cuprite, the linearity of the curve is maintained up to 450 °C. However, between $\approx 370$ and 450 °C, the samples containing copper ferrite exhibit a nonlinear behavior. The nonlinearity at the higher temperature is only visible during heating (hysteresis loop visible on Fig. 4b for the pure CuFe$_2$O$_4$ sample) and could be either due to the approach of the Curie temperature (as is seen in the case of all ferrites) or due to the structural change in copper ferrite. The Curie temperature of bulk copper ferrite is 455 °C [28]. The change of copper ferrite from tetragonal to cubic structure occurs in the temperature range 350–450 °C (Fig. 4b) in good agreement with temperatures reported in the literature [29]. The migration of Cu$^{2+}$ ions from octahedral to tetrahedral site has also been reported to occur above a temperature of 350 °C [30] and can be the origin of this phenomena. Above the temperature range of 370–420 °C, the linearity of the curve returns. It could be seen that the slope of the curve before and after the transition is different. This shows that there exist two regions with different activation energy, before and after the transition, which have already been reported for copper
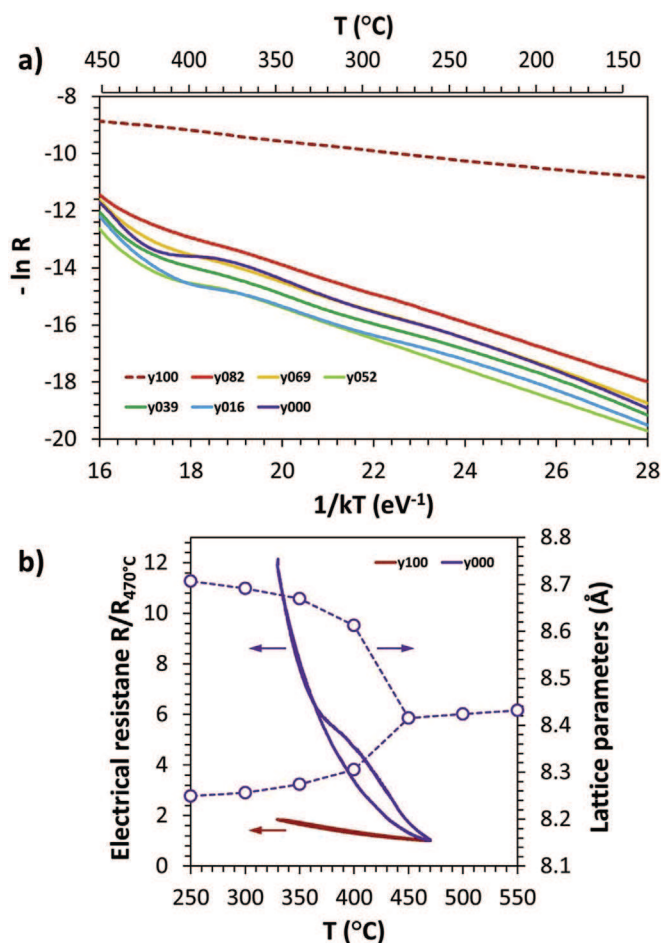
**Fig. 4.** a) Arrhenius plot of all samples. b) Normalized electrical resistance for the y000 and y100 samples during warming and cooling in the 330−470 °C range and corresponding lattice parameters a√2 and c for the y000 (CuFe₂O₄) phase versus temperature.

ferrite [31]. In our case, the activation energy remains in the same range before the transition, between 0.48 and 0.53 eV, for samples y000 to y082. However, after transition, the activation energy increased and was in the range 1.62−1.70 eV for samples y000 to y069. The increase in activation energy for sample y082 was lower than other composite samples and was 1.17 eV. It could also be seen that the activation energy of the sample y100 is 0.13 eV and is much smaller than that of other samples and slightly constant on all the temperature range.

The change in resistance and activation energy of pure copper oxide (y100) versus other composite samples could be explained as due to the difference in resistivity of the two phases (copper oxide is two order of magnitude less resistive than copper ferrite) and the limitation of the percolation pathway which takes into consideration the volume proportion of each phase in the system (geometric transition). For a simplified 2D model of percolation, considering connected squares which are usable in our device, the percolation threshold estimated by Monte Carlo method is at ≈ 60% in proportion of the conductive phase (CuO in our case) at the surface. One can note that this percolation threshold can also be increased by taking into consideration, the large porosity and large difference of grain sizes in between the two phases. Due to the difference of the density and molar mass between both materials (6.51 g cm⁻³ and 79.545 g mol⁻¹ for CuO and 5.42 g cm⁻³ and 139.232 g mol⁻¹ for CuFe₂O₄ respectively), this percolation

threshold corresponds to more than 85% in molar ratio of CuO. This limit is not achieved in our CuO/CuFe₂O₄ composite samples and corroborates the fact that for these composite samples, the electrical properties are driven by the electrical properties of CuFe₂O₄.

### 3.4. Type of charge carriers

In order to understand the type of charge carriers in copper ferrite, copper oxide and composites, the change in resistance of the sample with change in atmosphere was recorded. The change in resistance in argon atmosphere was compared with that in air. Fig. 5a gives the relative resistance at 350 °C of samples by the alternate insertion of air and argon in the interval of 1 h.

From Fig. 5a, for all the samples except pure copper oxide, i.e. for samples y000 − y082, it could be seen that the resistance increases with time in air atmosphere. On the contrary, with the insertion of Ar, the resistance of these samples decreases. For pure copper oxide (y100), the variations in air and argon atmospheres evolve in the opposite direction. All these variations are reproducible for many air/Ar cycles.

With the insertion of air, the resistance of samples y000 to y082 increases. This behavior is typical for n-type conductors. This is because the oxygen in air gets adsorbed on the surface as ions and accepts electron from the conduction band. This mechanism is schematically represented in Fig. 5b. The reduction of the number of electrons in the conduction band leads to the formation of depletion layer and thus the resistance of the sample increases. In case of pure copper oxide (y100), the resistance is found to decrease with the insertion of air. This shows that it is a p−type semiconductor. With the insertion of Ar, the electrons trapped by oxygen ions are released to conduction band and hence the resistance decreases for samples with electrons as the main charge carriers. For samples with holes as the main charge carriers (p-type), the release of trapped electrons, leads to reduction in the number of holes and hence an increase in the resistance.

As a result, from Fig. 5a, we see that pure copper ferrite has n-type charge carriers, while copper oxide has p type carriers. All the composites also show the presence of n type carriers even with the increase in the concentration of copper oxide which confirms that all compositions between y000 and y089 remains under the percolation threshold as already mentioned.

### 3.5. CO₂ sensing

All the nanoporous powder samples were tested for the response towards CO₂ with the corresponding fabricated device. The best operating temperature of the samples were studied by measuring the response at various temperatures from 200 to 400 °C. As a representative example, the typical variation of the resistance obtained for the sample y016 at different operating temperature is shown in Fig. 6a. The response (S = ΔR/R_air) was calculated by subtracting the base line corresponding to air from each curve. The response obtained at various operating temperature is shown in Fig. 6b.

From Fig. 6a, it is evident that the resistance of the sample decreases with increase in the operating temperature. It is also clear that the resistance of the sample always increases with the insertion of CO₂. From Fig. 6b, it could be seen that the response of the sample towards CO₂ increases with the operating temperature, reaches a maximum at 350 °C and then decreases with the further increase in operating temperature. Thus the best response was obtained at a temperature of 350 °C. The shape of the curve in Fig. 6b resembles that of a bell shaped curve and is typical for such semiconducting gas sensing layers [32]. The temperature range in which the maximum sensing response will take place is dependent
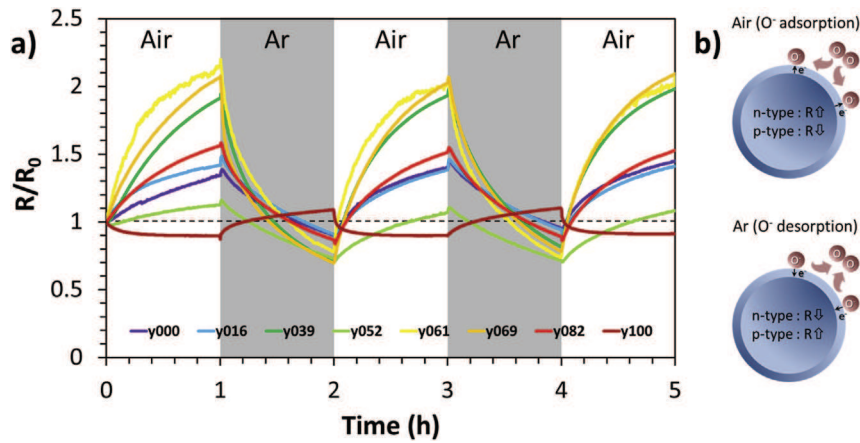
**Fig. 5.** a) Change in the relative resistance of samples, with the insertion of argon and air at 350 °C. b) Schematic representation of adsorption/desorption of oxygen in air and argon atmosphere.
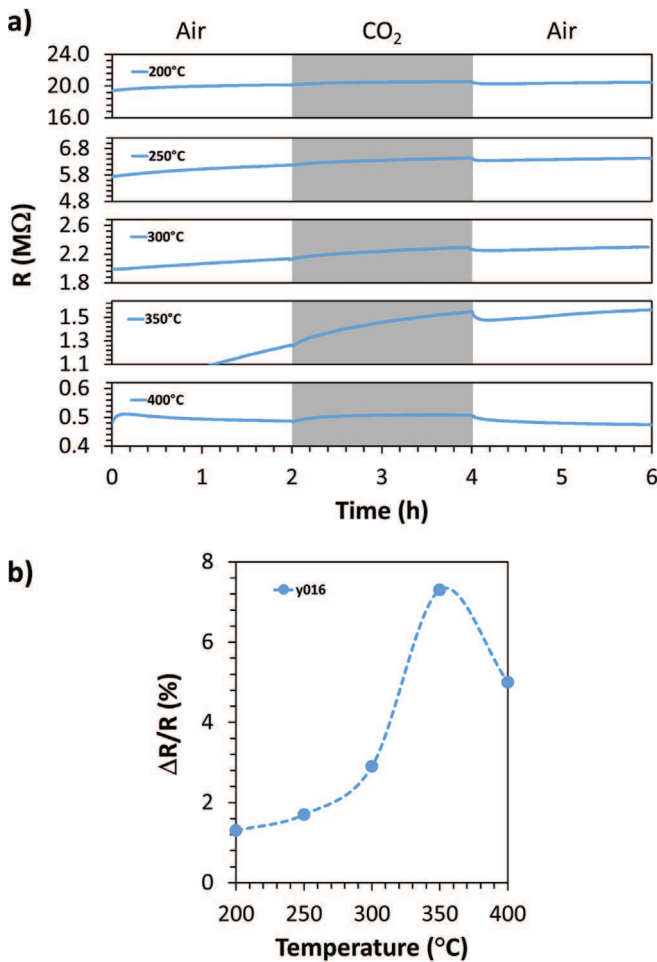


**Fig. 6.** For the y016 sample: a) resistance in the presence of air ($R_{air}$) and $CO_2$ ($R_{CO2}$) in the 200−400 °C temperature range and b) $\Delta R/R_{air}$ with at various operating temperature.

on adsorption-desorption mechanism of oxygen chemical species ($O_2^-$, $O^-$, $O^{2-}$), water molecules and target gas to be detected. As an example, the maximum sensing response of $SnO_2$ lies in the temperature range 280−450 °C [33]. In our case, the maximum response of all samples was obtained at 350 °C and is reported as a

function of the CuO content in Fig. 7.

From Fig. 7, it could be seen that the maximum response ($S \approx 10\%$) is obtained by pure copper ferrite sample (y000). The response of all the composite materials remains almost constant (within the error limit) and is independent of the proportion of cuprite phase except for sample y082 which has 82% cuprite phase. At this higher concentration of cuprite phase, there is a drastic decrease in the response. The response becomes negative for the pure cuprite sample.

It is remarkable to note from Fig. 7, that most of the samples exhibit a measurable response towards $CO_2$. These results show that copper ferrite can be sensitive to $CO_2$ without p-type counterpart. This is not common especially in powder samples. The decrease in the response for sample rich in cuprite content is in good agreement with the observations from Fig. 5a on the type of charge carrier. This in turn explains the presence of a negative response for the p-type semiconductor, cuprite. These results registered in air at 350 °C, confirm the oxidizing nature of $CO_2$ gas. Our results indicate that CuO may not be playing a crucial role in $CO_2$ sensing in the synthesized powder composites CuO-CuFe$_2$O$_4$. However, the low response of CuO may be due to the large size of CuO grains (1−2 μm) in comparison with those of copper ferrite (0.2−0.5 μm). This difference in the microstructure could affect the formation of p-n junction, which would otherwise enhance the sensing response towards $CO_2$ [18,20]. The larger grains of CuO would also exhibit lower sensing response in comparison with
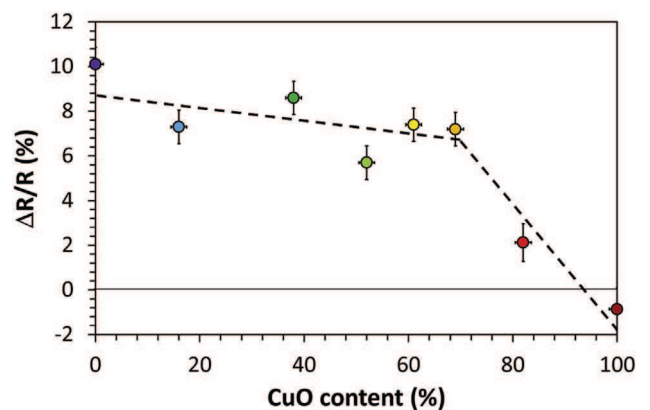


**Fig. 7.** $\Delta R/R_{air}$ as a function of the CuO content (y) measured at 350 °C. The dotted lines are only to guide the eye.

copper ferrite due to the reduced surface area. This latter point could be improved by reducing the processing temperature of the powder materials as the CuO has a lower size when treated at 300 °C, and shows a tremendous increase in size with further increase in temperature. However, it could be limited by the sintering process needed for the electrical measurements. Ongoing work concerns performance improvement by the physical mixing of the two components with similar morphology and by sintering the composite materials and devices at lower temperatures (500−600 °C).

## 4. Conclusion

Cuprite/copper ferrite oxide composites with controlled amount of CuO were synthesized using co-precipitation with oxalate precursors route. Thermal treatments at 780 °C under air were carried out for the phase purity. A novel simple and efficient technique was developed to fabricate ad-hoc devices for performing electrical and gas sensing performance of powder samples. The microstructure of the powder remained intact in the device. This made it possible to characterize the electrical properties (resistivity, activation energy, type of charge carrier) and $CO_2$ sensing behavior of the powder materials. This work reports for the first time the $CO_2$ response values of the whole $CuO/CuFe_2O_4$ composite material series. For the obtained microstructure, it shows that the amount of copper oxide does not contribute to improve the $CO_2$ sensing properties of the $CuFe_2O_4$ alone.

## References

[1] P.Barquinha, R.Martins, L.Pereira, E.Fortunato, Transparent Oxide Electronics : from Materials to Devices, Wiley Ed., ISBN: 978-0-470-68373-6.

[2] G. Fine, L. Cavanagh, A. Afonja, R. Binions, Metal Oxide Semi-Conductor gas sensors in environmental monitoring, Sensors 10 (2010) 5469−5502.

[3] Q. Zhang, K. Zhang, D. Xu, G. Yang, H. Huang, F. Nie, C. Liu, S. Yang, CuO nanostructures: synthesis, characterization, growth mechanisms, fundamental properties, and applications, Mater. Sci. 60 (2014) 208−337.

[4] C. Alexiou, R.J. Schmid, R. Jurgons, M. Kremer, G. Wanner, C. Bergemann, E. Huenges, T. Nawroth, W. Arnold, F.G. Parak, Targeting cancer cells: magnetic nanoparticles as drug carriers, Eur. Biophys. J. 35 (2006) 446−450.

[5] T. Ahmad, H. Bae, Y. Iqbal, I. Rhee, S. Hong, Y. Chang, J. Lee, D. Sohn, Chitosan-coated nickel-ferrite nanoparticles as contrast agents in magnetic resonance imaging, J. Magn. Magn. Mater. 381 (2015) 151−157.

[6] J.P. Fortin, C. Wilhelm, J. Servais, C. Ménager, J. Bacri, F. Gazeau, Size-sorted anionic iron oxide nanomagnets as colloidal mediators for magnetic hyperthermia, J. Am. Chem. Soc. 129 (2007) 2628−2635.

[7] A.B. Gadkari, T.J. Shinde, P.N. Vasambekar, Ferrite gas sensors, IEEE Sens. J. 11 (2011) 849−860.

[8] P.P. Hankare, S.D. Jadhav, U.B. Sankpal, R.P. Patil, R. Sasikala, I.S. Mulla, Gas sensing properties of magnesium ferrite prepared by co-precipitation method, J. Alloys Compd. 488 (2009) 270−272.

[9] S. Joshi, V.B. Kamble, M. Kumar, A.M. Umarji, G. Srivastava, Nickel substitution induced effects on gas sensing properties of cobalt ferrite nanoparticles, J. Alloys Compd. 654 (2016) 460−466.

[10] S.L. Darshane, R.G. Deshmukh, S.S. Suryavanshi, I.S. Mulla, Gas-sensing properties of zinc ferrite nanoparticles synthesized by the Molten-Salt route, J. Am. Ceram. Soc. 91 (2008) 2724−2726.

[11] G.V. Gopal Reddy, S.S. Manorama, V.J. Ra, Preparation and characterization of ferrites as gas sensor materials, J. Mater. Sci. Lett. 19 (2000) 775−778.

[12] A. Chapelle, M. Yaacob, I. Pasquet, L. Presmanes, A. Barnabé, P. Tailhades, J. Du Plessis, K. Kalantar-Zadeh, Structural and gas-sensing properties of CuO−$Cu_x$$Fe_{3-x}$$O_4$ nanostructured thin films, Sens. Actuat. B Chem. 153 (2011) 117−124.

[13] T.P. Sumangala, C. Mahender, A. Barnabé, N. Venkataramani, S. Prasad, Structural, magnetic and gas sensing properties of nanosized copper ferrite powder synthesized by sol gel combustion technique, J. Magn. Magn. Mater. 418 (2016) 48−53.

[14] T. Hu, X. Chu, F. Gao, Y. Dong, W. Sun, L. Bai, Acetone sensing properties of reduced graphene oxide−$CdFe_2O_4$ composites prepared by hydrothermal method, Mater. Sci. Semicond. Process. 34 (2015) 146−153.

[15] N. Patel, K. Makhija, C. Panchal, Fabrication of carbon dioxide gas sensor and its alarm system using indium tin oxide (ITO) thin films, Sens. Actuat. B Chem. 21 (1994) 193−197.

[16] U. Hoefer, G. Kuhner, W. Schweizer, G. Sulz, K. Steiner, CO and $CO_2$ thin-film $SnO_2$ gas sensors on Si substrates, Sens. Actuat. B Chem. 22 (1994) 115−119.

[17] A. Marsal, G. Dezanneau, A. Cornet, J. Morante, A new $CO_2$ gas sensing material, Sens. Actuat. B Chem. 95 (2003) 266−270.

[18] T. Ishihara, K. Kometani, Y. Mizuhara, Y. Takita, Mixed oxide capacitor of CuO/$BaTiO_3$ as a new type $CO_2$ gas sensor, J. Am. Ceram. Soc. 75 (1992) 613−618.

[19] T. Ishihara, K. Kometani, Y. Nishi, Y. Takita, Improved sensitivity of CuO/$BaTiO_3$ capacitive-type $CO_2$ sensor by additives, Sens. Actuat. B Chem. 28 (1995) 49−54.

[20] J. Herran, G.G. Mandayo, E. Castano, Solid state gas sensor for fast carbon dioxide detection, Sens. Actuat. B Chem. 129 (2008) 705−709.

[21] Z. Jiao, F. Chen, R. Su, X. Huang, W. Liu, J. Liu, Study on the characteristics of Ag doped CuO-$BaTiO_3$ $CO_2$ sensors, Sensors 2 (2002) 366.

[22] A. Chapelle, F. Oudrhiri-Hassani, L. Presmanes, A. Barnabé, P. Tailhades, $CO_2$ sensing properties of semiconducting copper oxide and spinel ferrite nanocomposite thin films, Appl. Surf. Sci. 256 (2010) 4715−4719.

[23] H.J. Kim, J.H. Lee, Highly sensitive and selective gas sensors using p-type oxide semiconductors: Overview, Sens. Actuat. B Chem. 192 (2014) 607−627.

[24] L.F. Silva, V.R. Mastelaro, A.C. Catto, C.A. Escanhoela, S. Bernardini, S.C. Zilio, E. Longo, K. Aguir, Ozone and nitrogen dioxide gas sensor based on a nanostructured $SrTiFe_{0.15}O_3$ thin film, J. Alloys Compd. 638 (2015) 374−379.

[25] A. Singh, A. Singh, S. Singh, P. Tandon, B.C. Yadav, R.R. Yadav, Synthesis, characterization and performance of zinc ferrite nanorods for room temperature sensing applications, J. Alloys Compd. 618 (2015) 475−483.

[26] K. Kiryukhina, H. Le Trong, Ph. Tailhades, J. Lacaze, V. Baco, M. Gougeon, F. Courtade, S. Dareys, O. Vendier, L. Raynaud, Silver oxalate-based solders: new materials for high thermal conductivity microjoining, Scr. Mater. 68 (2013) 623−626.

[27] I. Madsen, N. Scarlett, L. Cranswick, T. Lwin, Outcomes of the International union of crystallography commission on powder diffraction. Round Robin on quantitative phase analysis: samples 1a to 1h, J. Appl. Cryst. 34 (2002) 409−426.

[28] J. Smit, H.P.J. Wijn, Ferrites: Physical Properties of Ferrimagnetic Oxides in Relation to Their Technical Applications, Philips' Technical Library, Eindhoven, The Netherlands, 1959.

[29] X.X. Tang, A. Manthiram, J.B. Goodenough, Copper ferrite revisited, J. Solid State Chem. 79 (1989) 250−262.

[30] P. Tailhades, C. Villette, A. Rousset, G.U. Kulkarni, K.R. Kannan, C.N.R. Rao, M. Lenglet, Cation migration and coercivity in mixed copper−cobalt spinel ferrite powders, J. Solid. State Chem. 141 (1998) 56−63.

[31] K.S.R.C. Murthy, S. Mahanty, J. Ghose, Phase-transition studies on copper ferrite, Mat. Res. Bull. 22 (1987) 1665−1675.

[32] S. Ahlers, G. Muller, T. Doll, A rate equation approach to the gas sensitivity of thin film metal oxide materials, Sens. Actuat. B Chem. 107 (2005) 587−599.

[33] J.F. McAleer, P.T. Moseley, J.O.W. Norris, D.E. Williams, Tin dioxide gas sensors Part 1.-Aspects of the surface chemistry revealed by electrical conductance variations, J. Chem. Soc. Faraday Trans. I 83 (1987) 1323−1346.